Check for updates

Chemical-to-mechanical molecular computation using DNA-based motors with onboard logic

Selma Piranej[1], Alisina Bazrafshan[1] and Khalid Salaita [1,2] ✉

DNA has become the biomolecule of choice for molecular computation that may one day complement conventional silicon-based processors. In general, DNA computation is conducted in individual tubes, is slow in generating chemical outputs in response to chemical inputs and requires fluorescence readout. Here, we introduce a new paradigm for DNA computation where the chemical input is processed and transduced into a mechanical output using dynamic DNA-based motors operating far from equilibrium. We show that DNA-based motors with onboard logic (DMOLs) can perform Boolean functions (NOT, YES, AND and OR) with 15 min readout times. Because DMOLs are micrometre-sized, massive arrays of DMOLs that are identical or uniquely encoded by size and refractive index can be multiplexed and perform motor-to-motor communication on the same chip. Finally, DMOL computational outputs can be detected using a conventional smartphone camera, thus transducing chemical information into the electronic domain in a facile manner, suggesting potential applications.

One of the hallmarks of living systems is their ability to autonomously detect chemical inputs and process this chemical information to execute sophisticated functions such as locomotion[1]. For example, *Escherichia coli* switches the rotation of its flagella in response to nutrient concentrations. Creating synthetic systems that recapitulate the sense–process–respond capability of living systems is desirable as it would represent an important step toward next-generation sensors, computational devices and molecular robotics.

The most promising synthetic systems that demonstrate aspects of sensing, computation and actuation at the molecular scale rely on engineering nucleic acids. This is because of the highly predictable kinetics and thermodynamics of Watson–Crick–Franklin base pairing and the availability of triggered reactions, such as toehold-mediated strand displacement (TMSD)[2–5] and the hybridization chain reaction[6–9]. In particular, the TMSD reaction has been used in the construction of dynamic DNA nanostructures that process molecular inputs and produce specific responses[4,10–13]. For example, Seelig et al. demonstrated that nucleic acid TMSD logic gates can sense, process and release output oligonucleotides to generate a fluorescence signal[14]. Qian and colleagues later applied the TMSD reaction to create a nucleic acid 'robot' that undertakes a two-dimensional random walk to sort DNA[15]. More recently, Cherry and Qian used TMSD circuitry to create a 'winner-takes-all' neural network that exhibits autonomous behaviour[16]. In all these examples, the logic gates use binary-encoded molecules as input (present = 1, absent = 0) and optical or electrochemical signals as output (high = 1, low = 0)[14,17–20]. To date, the primary output of DNA computing systems is fluorescence[21–25]. Less common detection methods include single-molecule readouts, such as transmission electron microscopy and atomic force microscopy, to detect nanostructure translocation along a scaffold[26–28]. Transducing the output of DNA computation into microscopic or macroscopic responses that parallel the input-triggered locomotion of living systems may become useful for real-world applications.

In this study we addressed this challenge by engineering DNA-based motors with 'onboard' logic (DMOLs) that transduce chemical information into mechanical output in the form of macroscopic locomotion. DMOLs take advantage of rolling DNA-based motors that move at micrometre-per-minute speeds with high endurance (up to millimetres)[29,30]. The motors comprise a single-stranded DNA (ssDNA)-coated particle that hybridizes to complementary RNA immobilized on a planar chip (Fig. 1). The motors move upon addition of ribonuclease H (RNaseH) as it selectively hydrolyses RNA duplexed with DNA but is inactive towards single-stranded RNA (ssRNA). Thus, DNA–RNA hybridization at the motor–chip junction leads to rapid degradation of the RNA, which creates a chemical gradient of RNA. The free energy of RNA–DNA hybridization down this gradient drives motion. Rolling motors are not switches and do not move by random diffusion, rather they are bona fide motors. Most reported DNA motors are not formally processive machines. Rather, they are switches that toggle between two states and hence are unable to generate useful work such as motion[31,32].

DMOL speed is highly sensitive to the rate constants k_{cat}, k_{on} and k_{off} of RNA–DNA hydrolysis, hybridization and dissociation, respectively, and therefore motion is a readout of molecular input signals. Here, we first demonstrate the ability to stall motion using rationally designed nucleic acids. Next, we show that TMSD reactions can be used to engineer Boolean logic operations into motors, including DMOLs with NOT, YES, AND and OR gates. Because DMOLs produce motion rather than colour or fluorescence as the output, multiple unique DMOLs with different logic operations can be mixed on the same chip to process information in a parallelized manner. Multiplexed DMOLs were barcoded by fluorescence tagging, or by using motors with specific particle size and refractive index. DMOL size and refractive index can be detected using conventional bright-field microscopy, which is advantageous as this type of encoding potentially offers massive parallelization of information processing. Through the cascading of simple logic gates, we show communication between different DMOLs performing independent logic operations on the same chip. Finally, we demonstrate the accessibility of multiplexed DMOLs by processing five unique inputs using a smartphone camera. Given that DMOL outputs trigger rapid mechanical work in the form of macroscopic motion,

[1]Department of Chemistry, Emory University, Atlanta, GA, USA. [2]Wallace H. Coulter Department of Biomedical Engineering, Georgia Institute of Technology and Emory University, Atlanta, GA, USA. ✉e-mail: k.salaita@emory.edu
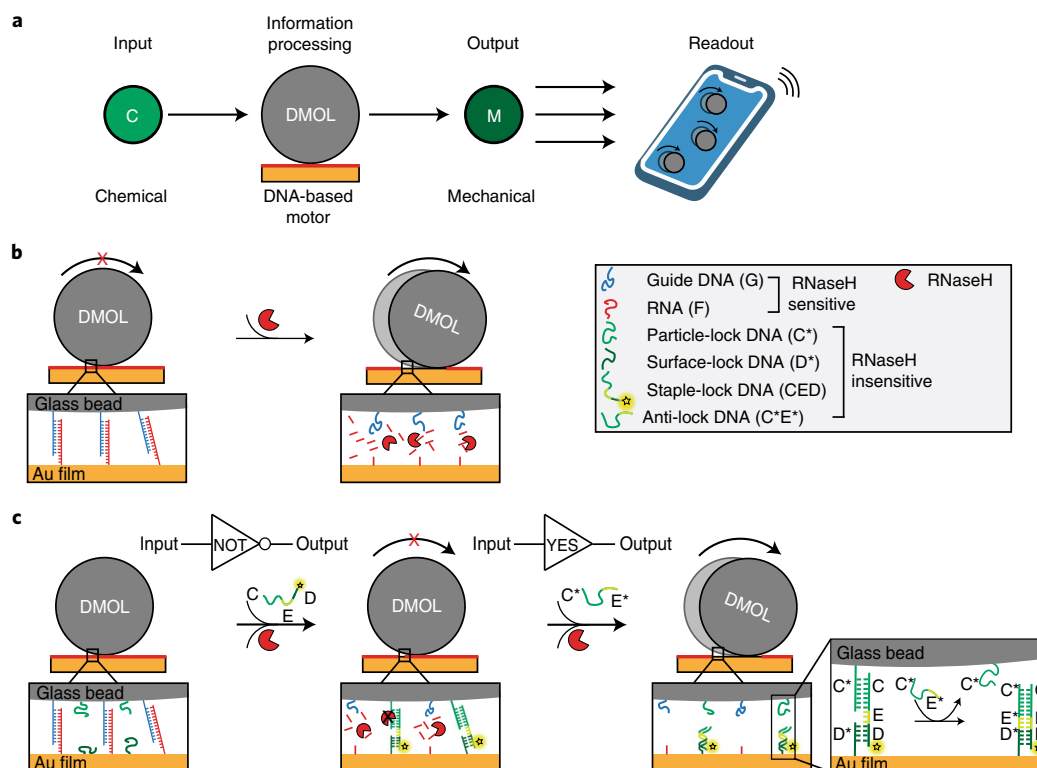
Fig. 1 | Schematic of DMOLs detecting the presence of a chemical input. a, Illustration of information-processing DMOLs sensing chemical input and transducing mechanical output that can be detected by smartphone readout. **b**, DMOLs modified with guide DNA (G) hybridize to complementary RNA fuel (F) on the chip. The motors remain stationary until the addition of RNaseH. In the presence of RNaseH, RNA is selectively cleaved and the motors roll forward through a burnt-bridge mechanism. **c**, In addition to guide DNA G, the DMOLs are functionalized with particle-lock DNA (C*). The chip is modified with a binary mixture of surface-lock DNA (D*) and F. Two different types of duplexed strands form upon the addition of staple-lock DNA (CED) strands: (1) G hybridizes with complementary F (degraded by RNaseH) and (2) CED hybridizes with C* on the particle and the surface-bound D* (RNaseH-resistant). In the presence of RNaseH, the particle remains stalled on the surface as it is mechanically locked by the DNA–DNA duplex formed (C*–CED–D*). The DMOLs serve as a NOT gate with the presence of CED stalling motion and its absence resulting in motion. An anti-lock DNA strand (C*E*) displaces CED from the particle through the TMSD reaction and engages motor motion. Acting as a YES gate, only the presence of an anti-lock DNA strand will result in motor motion.

readout can be performed in as little as 15 min, providing a facile method for DNA computation.

Design of DMOLs. We programmed the motors to develop stop-and-go motion in response to an external oligonucleotide input by conditioning motion to a TMSD reaction (Fig. 1). The particles were functionalized with the ssDNA guide (G), which binds to complementary ssRNA fuel (F) on the chip surface (Supplementary Fig. 1 and Supplementary Table 1 for all oligonucleotide sequences used in this study). The motor and chip surface were also modified with ssDNA that can form stable lock complexes to stall the motors. The 'onboard logic' requires oligonucleotide components that must be surface-anchored to generate resistive forces in excess of 100 pN that lead to stalling[33]. Therefore, the lock complex comprised ssDNA on the motor (C*), ssDNA on the chip (D*) and a complementary strand that binds to both C* and D* with an internal unbound ten-nucleotide toehold domain E (strand CED), as shown in Fig. 1c. The lock complex is insensitive to RNaseH hydrolysis and hence stalls motion in situ as it assembles at the junction between the motor and the chip surface. We hypothesized that displaying C*–CED on the motor along with complementary D* on the chip surface would lead to stalling (Fig. 1c). In this case, translocation requires mechanical shearing of multiple lock complexes, which exceeds the >100 pN force generation capacity of these motors[33]. Because motion is ultrasensitive to the binding events at the motor–chip

junction, the motor responds in a manner that is effectively binary to the lock complex, which lends itself to using motion as a digital output Boolean response: motion = 1 and stalling = 0. In Fig. 1c, for example, the motor behaves as a NOT gate, where the presence of the CED (input = 1) abrogates motion and output = 0. Conversely, the absence of CED (input = 0) rescues motion (output = 1). Note that the starting state of all motors described in this work is a NOT gate.

In principle, displacement of the CED from the motor surface prevents the formation of the lock complexes and rescues motion. In Fig. 1c, the presence of an anti-lock DNA (C*E*), input = 1, leads to motion, output = 1. The converse is true, and the absence of C*E*, input = 0, leads to stalling, output = 0. This type of Boolean operation is a YES gate (buffer gate), and CED release is driven by C*E* binding (Fig. 1c) because of the net gain of ten base pairs in the toehold domain[2].

To test the NOT/YES gate described above, we modified gold films with a binary mixture of two oligonucleotides, F and D* (Supplementary Fig. 1). The total oligonucleotide density on the chip surface was ~50,000 molecules μm^{-2}, and in initial experiments we introduced 1% D* and 99% F. Note that the F was tagged with cyanine dye Cy3 to map RNA hydrolysis using fluorescence microscopy. The motors (5 μm silica particles) were modified with 90% G and 10% CED at an overall DNA density of ~91,000 molecules μm^{-2} (ref. [33]; Supplementary Fig. 2). To visualize and

quantify TMSD, CED was tagged with cyanine dye Cy5. We call these particles DMOL1 in subsequent discussion. Upon the addition of CED, DMOL1 was first immobilized on the chip surface through D*–D and G–F hybridization. Addition of RNaseH led to a small but detectable motion (Fig. 2a). Despite the small translocation distances, we still observed consumption of Cy3-tagged F in the wake of the moving motors. CED-Cy5 oligo-colocalized with the motors, confirming that the CED staple lock remained bound during this experiment (Fig. 2a). Increasing the observation time to $t = 1$ h after RNaseH addition did not substantially increase displacement, as the locked particles showed 2.9 ± 2.3 µm ($n = 100$ particles) motion (Fig. 2b). Furthermore, DMOLs lacking staple-lock DNA continued rolling on the surface with high displacements even at $t = 5$ h after RNaseH addition (Supplementary Fig. 3). This confirms that the CED lock complex irreversibly stalls motion through specific DNA–DNA hybridization.

We next tested whether input C*E* can rescue DMOL1 motion. Here, we used 1 µM C*E* for 1 h prior to initiating motion with RNaseH (Supplementary Fig. 4). We observed an increase in the track length accompanied by a decrease in motor Cy5 intensity, confirming computation of the YES gate through TMSD-gated motion (Fig. 2a and Supplementary Video 1). Using the Cy3 depletion tracks from $n > 100$ motors, we found that the motor displacement increased from 2.3 ± 2.3 to 14.4 ± 7.6 µm at $t = 30$ min after the addition of C*E* (Fig. 2b). Similarly, motors lacking CED displayed track lengths of 11.5 ± 6.2 µm at $t = 30$ min (Supplementary Fig. 5a). Plots of motor Cy5 intensity show that TMSD displaces >90% of the staple-lock strand (Fig. 2c). Bright-field particle tracking confirmed that anti-lock C*E* rescued motion and increased motor speed up to 2 µm min^{-1} from 0.25 µm min^{-1} (Supplementary Fig. 5b).

To further enhance the fidelity of the DMOL response we screened staple-lock and surface-lock DNA densities, as the initial conditions with 10% staple-lock CED and 1% surface-lock D* showed incomplete stalling of DMOL1. We hypothesized that if we increased D* and CED density, or if we increased their rupture force, we could more effectively stall the motor while providing sufficient fuel RNA density and polyvalency to maintain processive and rapid motion. We previously showed that three or more 15mer DNA locks in a shearing geometry are required for stalling[33]. Thus, the mechanical stability and density of the locks are important determinants of the signal-to-noise (S/N) ratio of our system. We explored four DMOL1 staple-lock/surface-lock densities: (1) 10% staple-lock/1% surface-lock, (2) 10% staple-lock/5% surface-lock, (3) 50% staple-lock/1% surface-lock and (4) 50% staple-lock/5% surface-lock. Note that lock densities of >50% led to motor dissociation (data not shown) and bounded the parameter space tested. We measured both the track length and fluorescence intensity of the Cy5-labelled DMOLs with and without the

addition of anti-lock DNA (Fig. 2d and Supplementary Fig. 5c,d). To compare DMOL performance, we inferred the S/N of the logic gates based on the ratio of the track length with anti-lock DNA normalized by the track length of motors lacking anti-lock. DMOLs were also compared in terms of the ratio of the Cy5 intensity with and without anti-lock (Fig. 2d). DMOLs with 50% staple-lock/5% surface-lock showed the greatest S/N (Fig. 2d). This was mostly due to the suppression of motion in the absence of anti-lock, which was 0.4 ± 0.2 µm (Fig. 2b). Analysis of particle speed using bright-field videos confirmed this conclusion (Supplementary Fig. 5b). Taken together, we selected the 50% staple-lock/5% surface-lock DMOL design for subsequent experiments as these motors displayed greater fidelity.

To test the reversibility of Boolean operations, we modified the staple-lock DNA on DMOL1 to include a ten-nucleotide terminal toehold. As illustrated in Fig. 2e, the fluorescein (FAM)-tagged staple-lock DNA stalls DMOL1 while the anti-lock DNA rescues the motion of DMOL1 on the same chip. Fluorescence microscopy confirmed that the staple-lock DNA stalls DMOL1 while the anti-lock DNA rescues motion (Fig. 2f,h). Ensemble particle tracking of $n > 100$ DMOLs (taken at $t = 30$ min) showed that we stalled and recovered motion between NOT/YES gates in the two cycles (Fig. 2g,h). In principle, many more cycles can occur as the TMSD is reversible.

Computation of AND gate. Next, we designed and demonstrated an AND-gated motor (DMOL2) using two different staple-lock DNA strands (CED and MND; Fig. 3a). When DMOL2 senses the two inputs (input = 1), it is unlocked resulting in locomotion (output = 1). In this design, input A displaces lock CED-Cy5, while input B displaces lock MND-FAM (Fig. 3a). The labels verified the TMSD reaction, as input A and input B led to the loss of Cy5 and FAM signals from DMOL2, respectively. When DMOL2 was added to a surface comprising 5% D*, the motors stalled, as shown in Fig. 3b. Addition of either input A or input B (1 µM) did not trigger any detectable tracks (Fig. 3b). Fluorescence images confirmed that inputs A and B were active in mediating TMSD (Fig. 3b): only when both inputs A and B were added did DMOL2 display motion (Supplementary Video 2). The track lengths for DMOL2 receiving input A (0.8 ± 0.7 µm) did not differ from the tracks with no input added (0.3 ± 0.2 µm; Fig. 3c). However, track lengths increased to 6.6 ± 2.2 µm with both inputs A and B. Input A led to an ~20-fold reduction in Cy5 intensity, while input B led to an ~10-fold decrease in the FAM signal (Fig. 3d). These fluorescence levels for DMOL2 were not different from background levels, indicating near quantitative removal of lock strands CED and MND. Taken together, these results confirm that DMOLs can be programmed to compute an AND gate by chemical-to-mechanical transduction.

Fig. 2 | Computation of NOT and YES gates. a, Representative fluorescence images along with the overlay images (at $t = 30$ min after RNaseH addition) show fluorescent Cy3-tagged RNA as well as Cy5-tagged DMOLs before (top) and after (bottom) the addition of anti-lock DNA. **b**, Track lengths for DMOLs modified with 10% staple-lock DNA and added to the chip with 1% surface-lock DNA (left) and for DMOLs modified with 50% staple-lock DNA and 5% surface-lock DNA (right). Track lengths were quantified 30 and 60 min before the addition of anti-lock DNA (−) as well as 30 min after the addition (+). In both DMOL designs, the track lengths increase in the presence of anti-lock DNA. **c**, Cy5 fluorescence intensity of the DMOLs (10% staple-lock DNA, 1% surface-lock DNA) 30 and 60 min before adding the anti-lock DNA (−) and 30 min after the addition (+). a.u., arbitrary unit. **d**, Ratios of the mean track length (left) and Cy5 fluorescence intensity (right) with (+) and without (−) anti-lock DNA with varying densities of staple-lock and surface-lock DNA. **e**, Scheme showing reversible YES/NOT gate operations with 1 µM anti-lock DNA (C*E*D*I*) rescuing motion and staple-lock DNA (CEDI) stalling motion. **f**, Representative fluorescence images and overlay images (at $t = 30$ min after RNaseH addition) show Cy3-tagged RNA as well as the FAM-staple-lock channel after the addition of staple-lock DNA (top) and anti-lock DNA (bottom). **g**, Ensemble DMOL trajectories ($n > 100$ DMOLs) plotted from the centre (0, 0) for two cycles of YES/NOT gate computation on the same chip. **h**, Net displacements from bright-field particle tracking (left) and the corresponding FAM fluorescence intensity (right) of the DMOLs in the presence of staple-lock/anti-lock DNA over two cycles. The green region represents DMOLs with output = 1 and the red region DMOLs with output = 0. The error bars represent the standard deviations of $n > 100$ DMOLs from three independent experiments. **$P = 0.0013$; ****$P < 0.0001$; ns, not statistically significant. **a,f**, The vertical colour bars indicate the minimum, median, and maximum values (a.u.) used to display the fluorescence images of DMOLs. We include these bars to note the quantitative changes in fluorescence intensity following logic gate operations.

Computation of OR gate. The OR gate function was designed such that either of two chemical inputs (input = 1) yields locomotion (output = 1). The OR gate motor (DMOL3) was functionalized with 10% C* and 90% guide DNA, G. DMOL3 was introduced to a chip with 5% surface-lock DNA, D*. The rationale for using a lower density of C* (particle lock) compared with the AND/YES gates, which had 50% C*, is because one of the inputs in the OR gate required that C* was occupied by binding to CED, and at high densities of CED, motors showed low processivity. As shown in Fig. 4a, lock CED is displaced from the particle by input A, thus leading to a decrease in particle Cy5 fluorescence. Conversely, lock

CED can also be displaced from the chip surface by input C, which maintains the CED lock on the particle but terminates its bond to the chip-anchored D*. As a result, the Cy5 fluorescence intensity of the particle remains the same with input C. As we expected, when no input was present, DMOL3 stalled on the surface (Fig. 4b). The addition of either input A or input C rescued motion. For example, input A led to an ~10-fold increase in track length from $0.5 \pm 0.4\,\mu m$ (no input) to $4.7 \pm 1.5\,\mu m$ (Fig. 4c). Likewise, input C triggered motion with track lengths of $4.1 \pm 1.0\,\mu m$. For comparison, DMOL3 motors lacking staple-lock CED displayed tracks of $4.1 \pm 1.4\,\mu m$ on a surface with 5% D*. Note that the track lengths for these motors
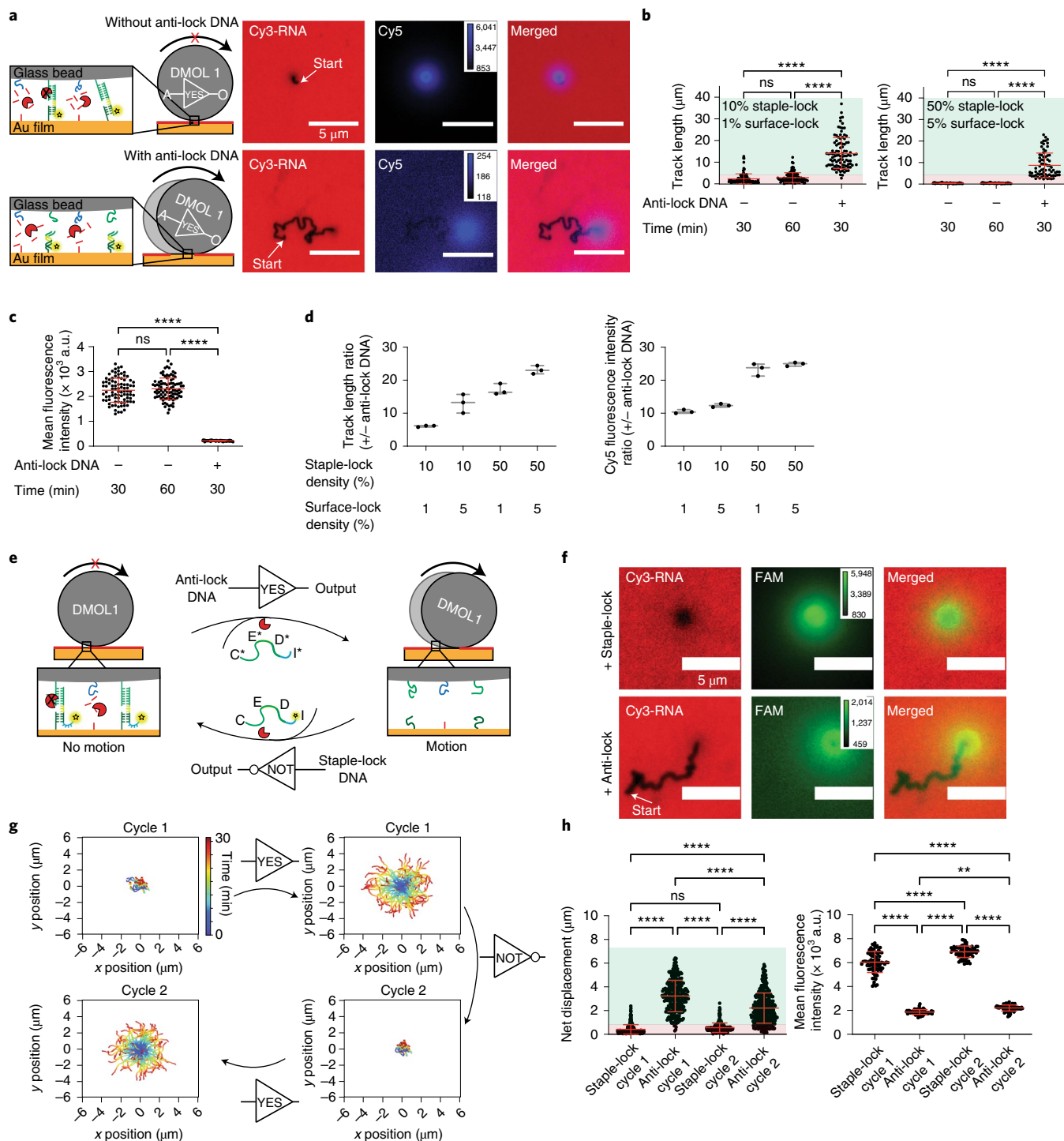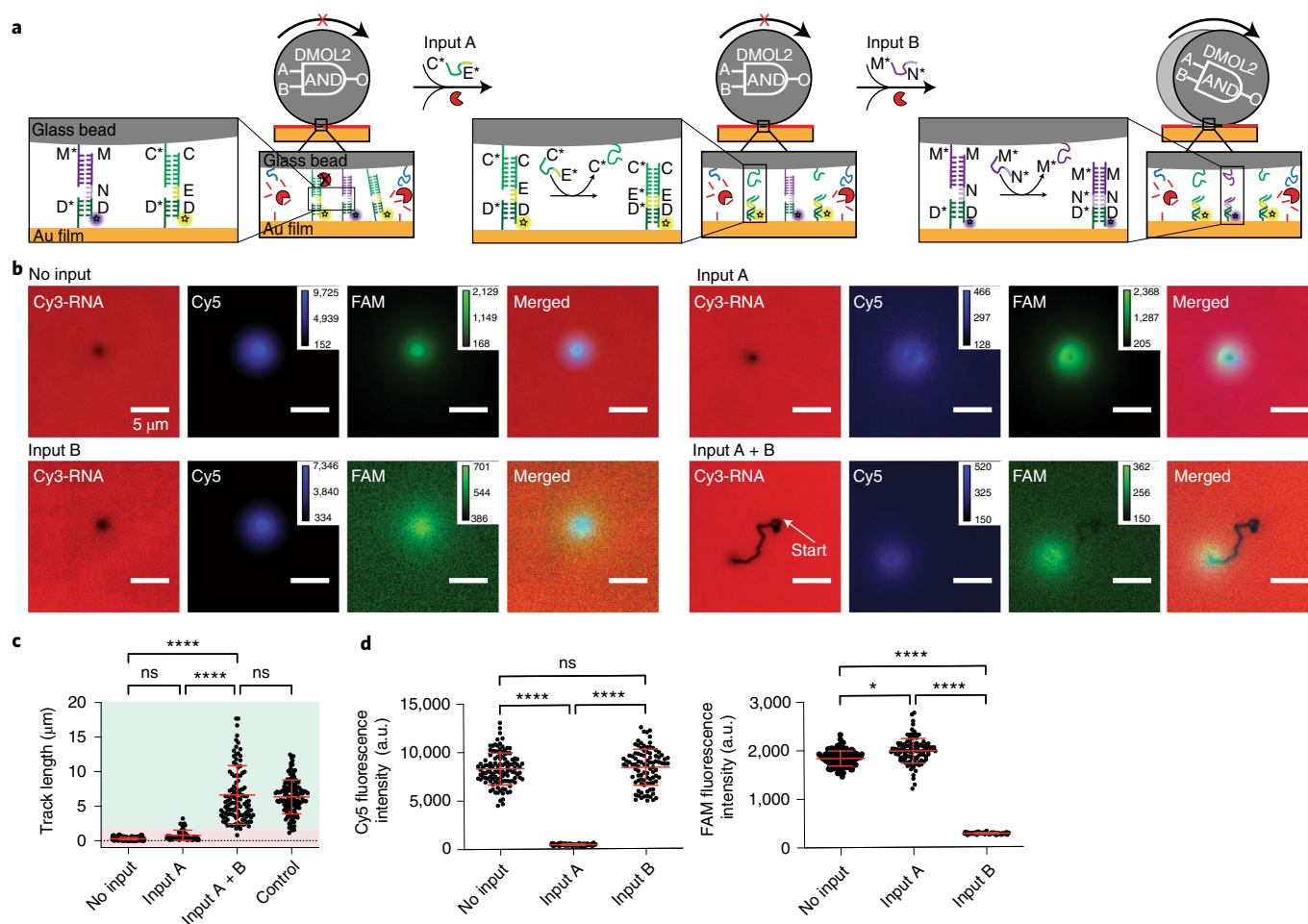
Fig. 3 | Computation of AND gate. a, Illustration of the AND gate for DMOL2, showing particle motion as output only when both inputs A and B are present. **b**, Representative Cy3, Cy5 and FAM fluorescence images along with overlay images (at $t = 30$ min after RNaseH addition) for DMOL2 with no input, input A, input B and input A + B. The addition of input A + B leads to an increase in Cy3 depletion track lengths and a decrease in Cy5 and FAM fluorescence. The vertical colour bars indicate the minimum, median, and maximum values (a.u.) used to display the fluorescence images of DMOLs. We include these bars to note the quantitative changes in fluorescence intensity following logic gate operations. **c**, Measured track lengths ($t = 30$ min) with no input, input A and input A + B. The track lengths for a control, without any staple lock present, are also shown. DMOLs remain stalled upon the addition of only one input; however, they are released from the surface when both inputs A and B are present, with the average track length measuring 6.6 ± 2.2 µm. The green region represents DMOLs with output = 1 and the red region DMOLs with output = 0. **d**, Cy5 (left) and FAM (right) fluorescence intensities of the DMOLs after 30 min with no input, input A or input B. A decrease in Cy5 fluorescence intensity is observed when input A is added as the locks functionalized with Cy5 are displaced from the particle. In a similar manner, a decrease in FAM fluorescence intensity is observed when input B is added as the locks functionalized with FAM are displaced from the particle. The error bars correspond to the standard deviations of $n > 100$ DMOLs from three independent experiments. *$P = 0.018$; ****$P < 0.0001$; ns, not statistically significant.

are shorter due to the smaller size of DMOL3 (3 µm)[29]. Confirming the TMSD reaction, input A led to a decrease in particle Cy5 fluorescence intensity as CED was displaced from the particle (Fig. 4d). Meanwhile, input C did not change the particle's fluorescence intensity, validating that the lock CED is displaced from the chip surface. Therefore, we have shown that with a careful design of nucleic acid lock domains, DMOLs can be programmed with OR gate function in a facile manner.

Multiplexing fluorophore-encoded DMOLs. More sophisticated computations require multiple orthogonal logic gates to operate in tandem and in sequence. Some of the advantages of DMOLs include their small size and ease of programmability, and thus there is the potential for carrying out multiple logical operations in a massive parallel fashion. To demonstrate parallel multiplexing where two independent DMOLs perform computations in the same pot, we aimed to integrate both YES- and AND-gated computing DMOLs

on the same chip. As a proof-of-concept, DMOLs were encoded with unique fluorophores to denote their identity. The CED lock sequence of the YES-gated DMOL (DMOL1) was tagged with Cy5 and the AND-gated DMOL (DMOL2) was tagged with Cy5 and FAM dyes that were conjugated to the CED and MND locks, respectively. Cy5-encoded DMOL1 will respond only to input A, whereas the FAM- and Cy5-encoded DMOL2 will respond to both inputs A and B (Fig. 5a). DMOL1 and DMOL2 were prepared and added to a chip at a 1:1 stoichiometry. Upon addition of input A, the DMOL1 tracks increased to 8.4 ± 4.9 µm in length (Fig. 5b) accompanied by Cy3-RNA depletion tracks and the loss of the Cy5 signal (Fig. 5c, Supplementary Fig. 6 and Supplementary Video 3). In contrast, DMOL2 remained stalled with input A (track lengths 0.3 ± 0.2 µm) and as expected the Cy5 signal decreased while the FAM signal was maintained (Fig. 5b,c). We next added input B to the same chip for 60 min and then collected images to monitor motion. The Cy5 and FAM channels showed a loss of signal for DMOL2, confirming lock
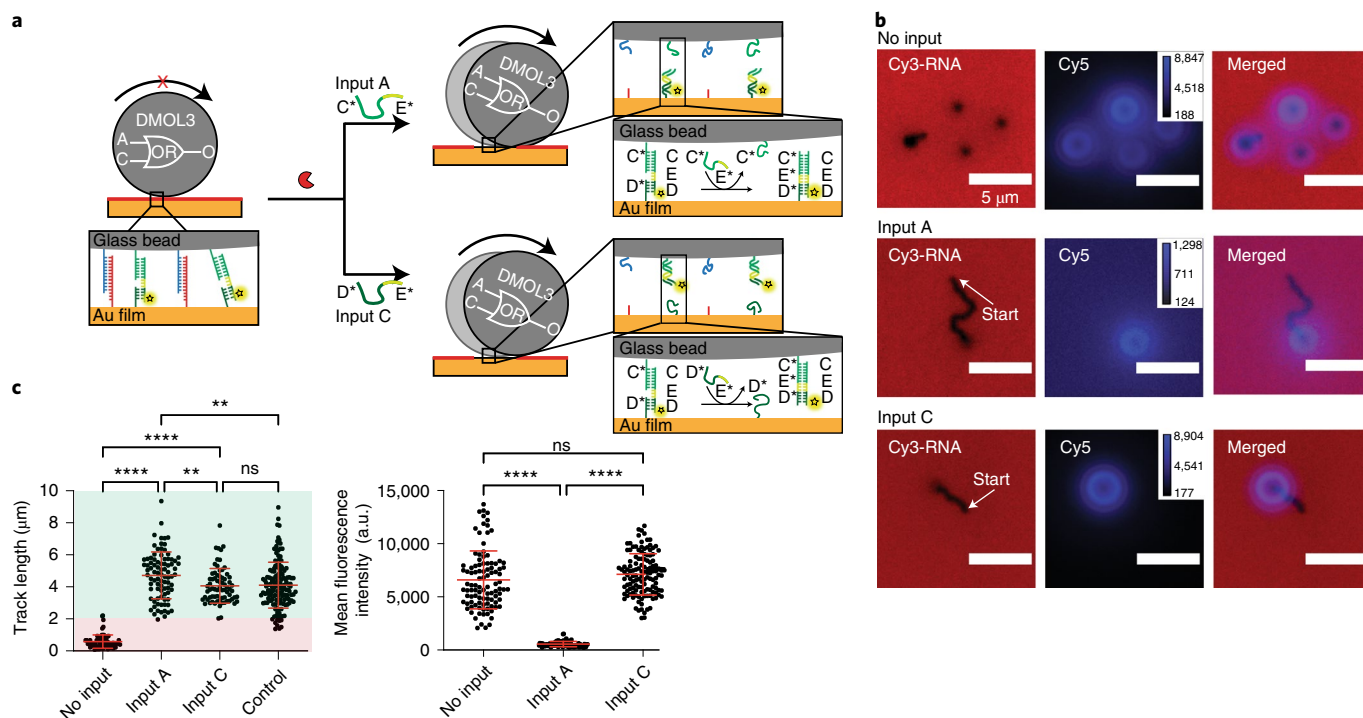
Fig. 4 | Computation of OR gate. a, Illustration of the OR gate showing particle motion as an output with either input A or C present. **b**, Representative Cy3 and Cy5 fluorescence images along with overlay images (at $t = 30$ min after RNaseH addition) for DMOL3 with no input, input A and input C. Depleted Cy3-RNA tracks are observed with either input A or C. The vertical colour bars indicate the minimum, median, and maximum values (a.u.) used to display the fluorescence images of DMOLs. We include these bars to note the quantitative changes in fluorescence intensity following logic gate operations. **c**, Measured track lengths (left) and fluorescence intensities (right) for DMOL3 after 30 min with no input, input A or input C. The track lengths for a control, without any staple lock present, are also shown. The DMOLs showed motion upon the addition of either input A (4.7 ± 1.5 μm) or input C (4.1 ± 1.0 μm). The green region represents DMOLs with output = 1 and the red region DMOLs with output = 0. A decrease in Cy5 fluorescence intensity is observed when input A is added as the locks labelled with Cy5 are displaced from the DMOL. However, no decrease in DMOL Cy5 intensity is observed upon the addition of input C as the labelled locks are displaced from the surface but remain on the particle. The error bars correspond to the standard deviations of $n > 100$ DMOLs from three independent experiments. **$P = 0.0015$; ****$P < 0.0001$; ns, not statistically significant.

displacement (Fig. 5c and Supplementary Fig. 6). DMOL2 tracks increased upon the addition of both inputs A and B. Confirming the specificity of multiplexed detection, both DMOL1 and DMOL2 stalled when only input B was introduced (Fig. 5b,c). DMOL2 only moved in the presence of both inputs A and B whereas input A only engaged DMOL1 motion. Thus, these results demonstrate that DMOLs can be multiplexed and parallelized to detect unique chemical inputs in the same chip.

DMOL-to-DMOL networking through cascading logic gates.
Now that we have established the ability to encode different DMOLs on the same chip and given that each DMOL operates as an independent 'agent', we next aimed to design DMOLs that can communicate through cascading logic gates. We leveraged the facile scalability and programmability of our architecture to design a two-layer YES–OR cascade, as illustrated in Fig. 5d and Supplementary Fig. 7. In this design, DMOL4 (5 μm silica sphere) is a YES gate and DMOL5

Fig. 5 | Encoding DMOLs to multiplex and demonstrate communication. a, Illustration depicting the computation of the YES gate by DMOL1 and the AND gate by DMOL2. DMOL1 moves when input A is present while DMOL2 moves when inputs A and B are present. **b**, Track lengths of the DMOLs after the addition of input A, input B or input A + B for the two different motors. DMOL1 motion is triggered upon the addition of input A whereas DMOL2 moves only in the presence of input A + B. The green regions represent DMOLs with output = 1 and the red regions DMOLs with output = 0. **c**, Representative Cy3, Cy5 and FAM fluorescence images along with overlay images (at $t = 30$ min after RNaseH addition). Cy3-RNA depletion tracks are observed for DMOL1 in the presence of input A and input A + B. The addition of input A also leads to a decrease in Cy5 fluorescence intensity. No Cy3 depletion tracks are observed for DMOL1 or DMOL2 in the presence of input B. The addition of input B also leads to a decrease in FAM fluorescence intensity. Input A + B engages motion for DMOL1 and DMOL2, as shown by the increase in Cy3 depletion tracks. The vertical colour bars indicate the minimum, median, and maximum values (a.u.) used to display the fluorescence images of DMOLs. We include these bars to note the quantitative changes in fluorescence intensity following logic gate operations. **d**, Schematic of a two-layer cascading logic circuit. DMOL4 (YES gate) was functionalized with 30% particle-lock C* and 70% G. The particle-lock density was reduced to 30% to accommodate the long length of the staple-lock oligonucleotide (83 nucleotides). DMOL5 (OR gate) was functionalized with 10% particle-lock M* and 90% G. **e**, Track lengths (top) and FAM fluorescence intensity (bottom) for DMOL4 and DMOL5 with no input, input D or input E. Both DMOL4 and DMOL5 engage in motion upon the addition of input D, whereas input E results in motion only for DMOL5. The green region represents DMOLs with output = 1 and the red region DMOLs with output = 0. A decrease in FAM fluorescence intensity for both DMOLs is observed when input D is added as the FAM-labelled locks are displaced from the DMOLs. Input E leads to a decrease in fluorescence only for DMOL5. The error bars correspond to the standard deviations of $n > 100$ DMOLs from three independent experiments. *$P = 0.018$; ****$P < 0.0001$; ns, not statistically significant.

(6 µm polystyrene sphere) is an OR gate. Both DMOL4 and DMOL5 were incubated with their respective FAM-tagged staple-lock DNA and added to a chip with 10% surface-lock DNA. In the absence of input, both DMOLs showed high FAM intensity and remained stalled (Fig. 5e and Supplementary Fig. 8a). When input D was added (input = 1, 10 µM), motion of both DMOL4 and DMOL5

was observed accompanied by a decrease in the FAM signal, confirming the loss of staple-lock DNA (output = 1). When DMOL5 alone was exposed to input D (1 µM), no motion was observed and FAM fluorescence remained the same, indicating that DMOL5 is responding to the output from DMOL4 (Supplementary Fig. 8b). Input E (input = 1, 1 µM) triggered DMOL5 motion (output = 1) but
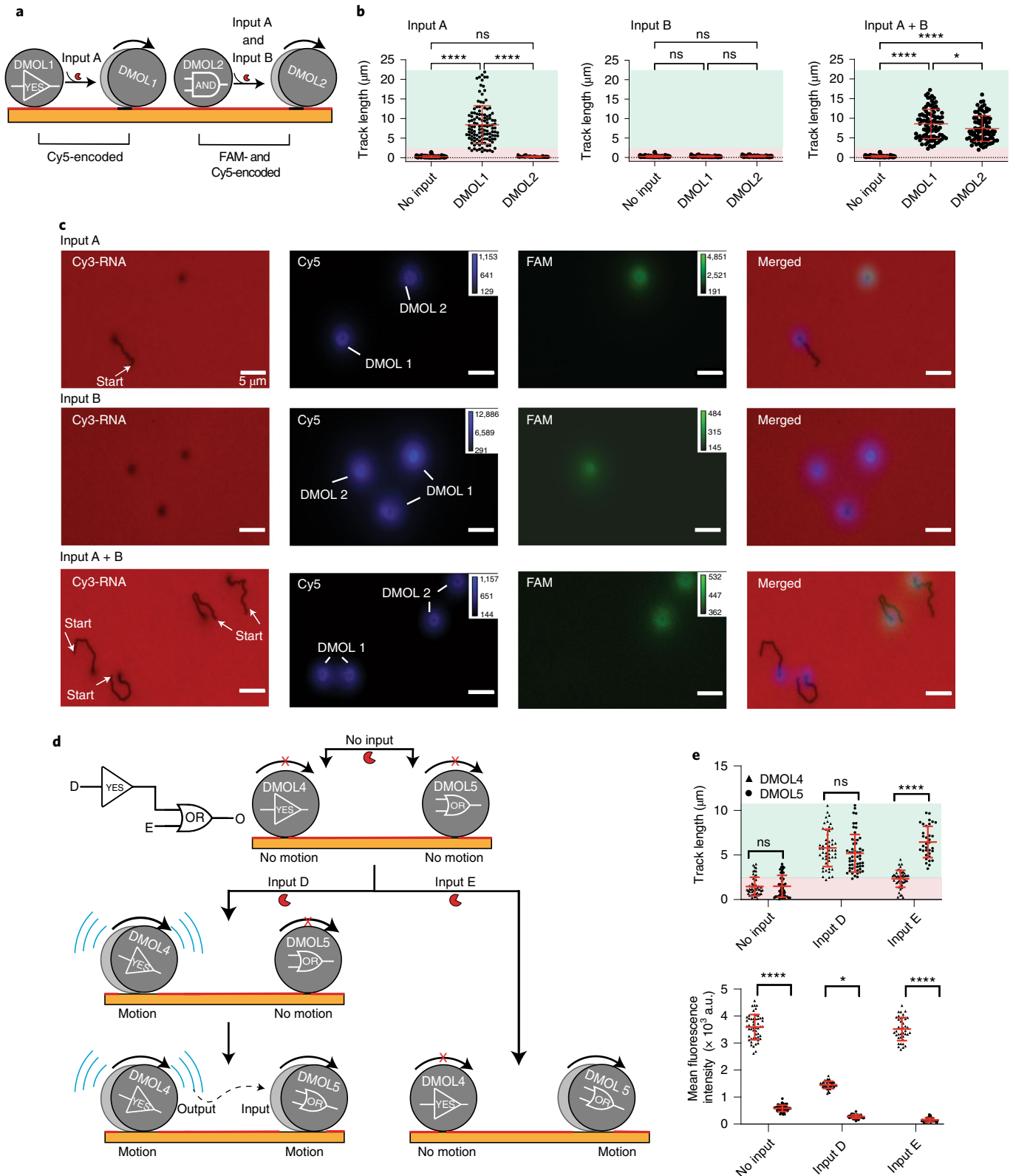
not DMOL4 motion (Fig. 5e and Supplementary Fig. 8a). Although not demonstrated here, the output of DMOL5 can then bind downstream another set of logic gates. Taken together, we have demonstrated communication between DMOLs by organizing the logic gates such that the output of one DMOL could serve as the input for another downstream DMOL.

Multiplexing with DMOLs by size and material. For molecular computing to one day complement the capabilities of traditional silicon-based computers, molecular systems need to be able to perform massive multiplexing of logic operations. The fluorophore-based encoding described above is limited to tens of unique multiplexing DMOLs because of the spectral bandwidth of unique fluorophores[34]. Another challenge is that chemical-to-mechanical transduction is currently being read out using fluorescence in a high-end microscope, which limits widespread adoption and portability. To address these issues we sought alternate encoding and readout strategies. One approach is the use of DMOLs of different size and material that can be detected through simple bright-field imaging (Fig. 6a). We chose to barcode the DMOLs based on size ranging from 3 to 6 μm and comprising materials such as silica and polystyrene, which are easily distinguished using bright-field imaging (Supplementary Fig. 9). Moreover, the micrometre size of the DMOLs and their micrometre displacements can be conveniently detected using a smartphone-based microscope. Figure 6a shows a representative bright-field image of three different DMOLs obtained using a smartphone camera. We encoded the DMOLs as follows: DMOL2 (two-input AND gate) was a 6 μm polystyrene bead, DMOL3 (OR gate) was a 3 μm polystyrene bead and DMOL6 (three-input AND gate) was a 5 μm silica bead. To test multiplexing, DMOL2, DMOL3 and DMOL6 were prepared and added to a chip at a 1:1:1 stoichiometry. As depicted in Fig. 6b, DMOL2 responds to input A + B, DMOL3 to input A or C, and DMOL6 to input A + B + F. Readout required the acquisition of time-lapse videos during 15 min following the addition of RNaseH. The trajectories of DMOL2, DMOL3 and DMOL6 were analysed by particle tracking by bright-field imaging and are shown in Fig. 6c after the addition of each input. When input A was added, DMOL3 moved along the surface with a net displacement of 1.1 ± 0.7 μm (Fig. 6c(i) and Supplementary Video 4). In contrast, DMOL2 and DMOL6 remained stalled (0.1 ± 0.1 and 0.1 ± 0.2 μm, respectively). When inputs A and B were added, DMOL2 and 3 moved 2.6 ± 0.9 μm and 0.9 ± 0.6 μm, respectively, while DMOL6 remained stalled (0.2 ± 0.1 μm; Fig. 6c(ii) and Supplementary Video 5). Input A + B + C once again rescued the motion of DMOL3 and DMOL2 (Fig. 6c(iii) and Supplementary Video 6). Input A + B + C + F triggered the motion of all DMOLs, displaying net displacements of 2.3 ± 1.1, 1.2 ± 0.7 and 1.7 ± 1.2 μm for DMOL2, DMOL3 and DMOL6, respectively (Fig. 6c(iv) and Supplementary Video 7). The Cy3-RNA depletion tracks formed by each DMOL are shown in Supplementary Fig. 10 along with the quantification of their track lengths and fluorescence intensities. These results show that DMOLs with different logic operations can be mixed on the same chip to process information in a parallelized manner. Importantly, bright-field readout allows DMOLs to convert chemical information into the modern electronic domain directly.

Conclusions

In this paper we have presented a method of molecular computation using DNA-based motors. We have shown that DMOLs can compute NOT, YES, AND and OR gates. Processing can be performed in series or in parallel with multiple uniquely encoded DMOLs. Specifically, the DMOLs respond to two inputs in series: at first, they are locked, producing no motion (NOT gate), but then a different input leads to motion (YES/AND/OR gate). Figures 5 and 6 show orthogonal motors operating in tandem. Processing agents operating in parallel and in series represent important components for building more complex computational systems. Although we have not extensively tested how the fidelity of DMOL processing responds with readout time, we have found that a 15 min time window provides multi-micrometre displacements and offers sufficient specificity for the proof-of-concept experiments shown here. In principle, longer readout times will enhance the fidelity of information processing ($\propto 1/t^{1/2}$). Nonetheless, 15 min readouts compare favourably with the state-of-the-art[35] and given that DMOLs operate in a parallel fashion, scaling additional operations will not require longer readout times.

We have demonstrated two types of barcoding for multiplexed DMOLs using either fluorophore-encoding or particles of different size and material. The latter type of encoding may offer upwards of thousands of unique barcodes. As a conservative estimate, tens of different microparticle materials have been reported, and each of these can be synthesized with tens to hundreds of distinguishable sizes and shapes. Additional channels of encoding are envisioned using recent advances in smartphone imaging[36,37]. Our facile and label-free approach addresses a big challenge for complex DNA computing systems, which is the readout of multiple outputs at the same time such as in parallel computing.

We also need to describe some of the caveats of DMOLs. For example, RNA is sensitive to environmental RNases that will deplete the fuel and diminish motion. The relatively slow kinetics of TMSD on surfaces is a bottleneck in terms of total assay time and faster reactions are needed to reduce information processing times. Communication between DMOLs, such as in cascading logic gates, is slow as the output signal from one gate is at a lower concentration and needs to diffuse across the chip to communicate with the next DMOL. Workarounds include the use of signal amplification techniques. Future advances in the chemistry and engineering of DMOLs will likely address these limitations.

Compared with previous molecular computation systems, our method has several advantages, including easy-to-detect locomotion output and shorter response times. As a corollary, the label-free method described in this work could be important in nucleic acid sensing and other applications. Also, the logic gate does not need to be 'on board' the motor; rather, a motion-based readout method can be integrated with any assay that generates oligonucleotide outputs. Thus, DMOLs allow the field of DNA computation to massively increase multiplexing capabilities by offering label-free readouts. Finally, we envision that DMOLs can be programmed to construct more complicated DNA-based networks for signal reception and processing, which is a key goal of bottom-up synthetic biology.

Fig. 6 | Size and material encoded DMOLs. a, Set-up of the smartphone microscope and a representative bright-field image of DMOL2, DMOL3 and DMOL6 with the trajectories shown for a time-lapse acquisition of 15 min (left). Plot showing the different sizes and materials of DMOL2 (6 μm polystyrene particle), DMOL3 (3 μm polystyrene particle) and DMOL6 (5 μm silica particle) (right). **b,** Schematic illustrating the computation of a two-input AND gate by DMOL2, an OR gate by DMOL3 and a three-input AND gate by DMOL6. **c,** Ensemble trajectories of different size- and material-encoded DMOLs as well as the corresponding net displacements 15 min after RNaseH addition with input A (i), input A + B (ii), input A + B + C (iii) and input A + B + C + F (iv). The green regions in the net displacement plots represent DMOLs with output = 1 and the red regions DMOLs with output = 0. The error bars correspond to the standard deviations of $n > 20$ DMOLs from three independent experiments. **P = 0.0015; ****P < 0.0001; ns, not statistically significant.
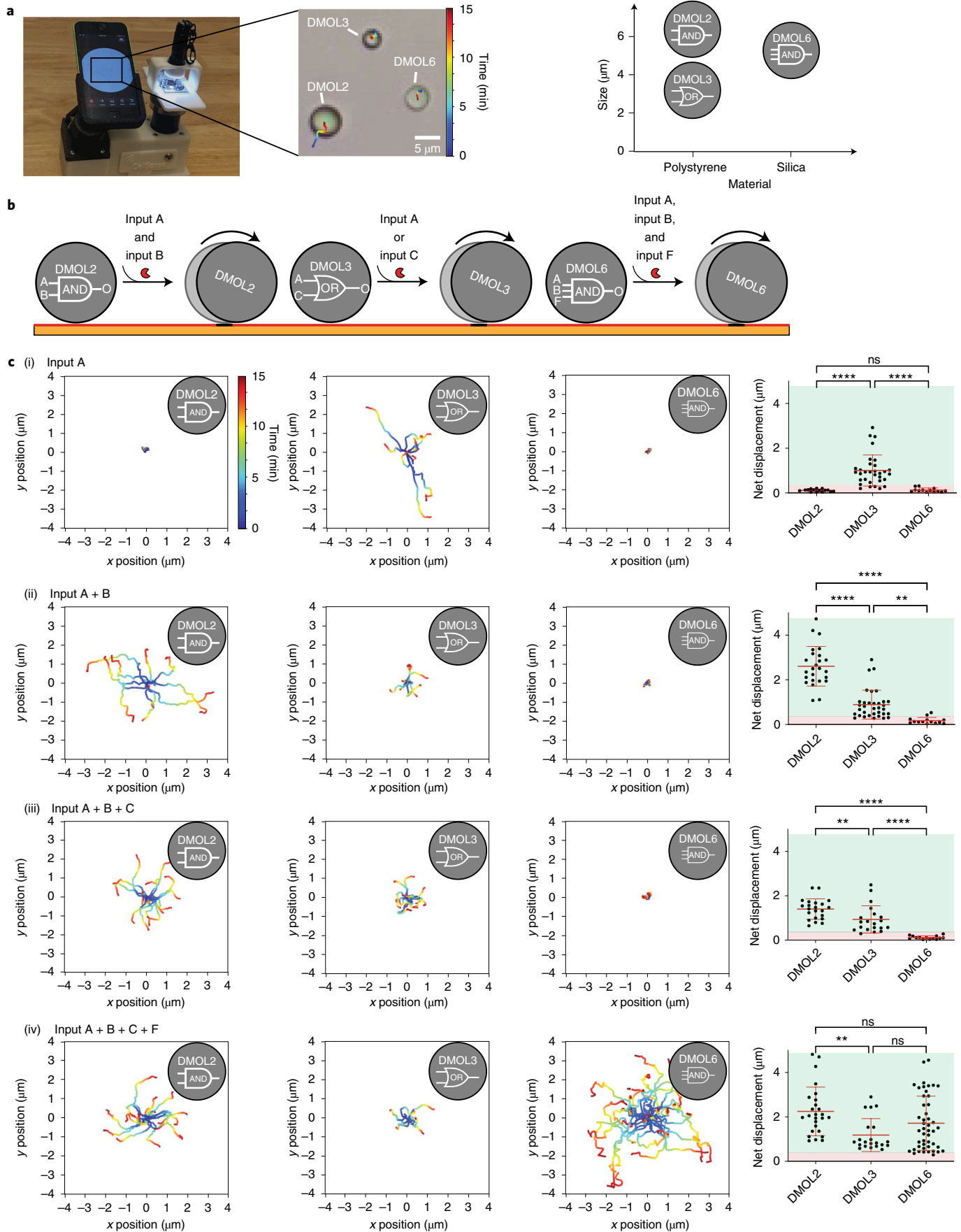
Online content

Any methods, additional references, Nature Research reporting summaries, source data, extended data, supplementary information, acknowledgements, peer review information; details of author contributions and competing interests; and statements of data and code availability are available at https://doi.org/10.1038/s41565-022-01080-w.

References

1. Wadhams, G. H. & Armitage, J. P. Making sense of it all: bacterial chemotaxis. *Nat. Rev. Mol. Cell Biol.* **5**, 1024–1037 (2004).
2. Srinivas, N. et al. On the biophysics and kinetics of toehold-mediated DNA strand displacement. *Nucleic Acids Res.* **41**, 10641–10658 (2013).
3. Genot, A. J., Zhang, D. Y., Bath, J. & Turberfield, A. J. Remote toehold: a mechanism for flexible control of DNA hybridization kinetics. *J. Am. Chem. Soc.* **133**, 2177–2182 (2011).
4. Yurke, B., Turberfield, A. J., Mills, A. P., Simmel, F. C. & Neumann, J. L. A DNA-fuelled molecular machine made of DNA. *Nature* **406**, 605–608 (2000).
5. Zhang, D. Y. & Seelig, G. Dynamic DNA nanotechnology using strand-displacement reactions. *Nat. Chem.* **3**, 103–113 (2011).
6. Dirks, R. M. & Pierce, N. A. Triggered amplification by hybridization chain reaction. *Proc. Natl Acad. Sci. USA* **101**, 15275–15278 (2004).
7. Augspurger, E. E., Rana, M. & Yigit, M. V. Chemical and biological sensing using hybridization chain reaction. *ACS Sens.* **3**, 878–902 (2018).
8. Ge, Z. et al. Hybridization chain reaction amplification of microRNA detection with a tetrahedral DNA nanostructure-based electrochemical biosensor. *Anal. Chem.* **86**, 2124–2130 (2014).
9. Bi, S., Chen, M., Jia, X., Dong, Y. & Wang, Z. Hyperbranched hybridization chain reaction for triggered signal amplification and concatenated logic circuits. *Angew. Chem. Int. Ed.* **54**, 8144–8148 (2015).
10. Qian, L. & Winfree, E. A simple DNA gate motif for synthesizing large-scale circuits. *J. R. Soc. Interface* **8**, 1281–1297 (2011).
11. Qian, L. & Winfree, E. Scaling up digital circuit computation with DNA strand displacement cascades. *Science* **332**, 1196–1201 (2011).
12. Song, X., Eshra, A., Dwyer, C. & Reif, J. Renewable DNA seesaw logic circuits enabled by photoregulation of toehold-mediated strand displacement. *RSC Adv.* **7**, 28130–28144 (2017).
13. Benenson, Y. et al. Programmable and autonomous computing machine made of biomolecules. *Nature* **414**, 430–434 (2001).
14. Seelig, G., Soloveichik, D., Zhang, D. Y. & Winfree, E. Enzyme-free nucleic acid logic circuits. *Science* **314**, 1585–1588 (2006).
15. Thubagere, A. J. et al. A cargo-sorting DNA robot. *Science* **357**, eaan6558 (2017).
16. Cherry, K. M. & Qian, L. Scaling up molecular pattern recognition with DNA-based winner-take-all neural networks. *Nature* **559**, 370–376 (2018).
17. Zhou, C., Geng, H., Wang, P. & Guo, C. Programmable DNA nanoindicator-based platform for large-scale square root logic biocomputing. *Small* **15**, 1903489 (2019).
18. Benenson, Y. Biomolecular computing systems: principles, progress and potential. *Nat. Rev. Genet.* **13**, 455–468 (2012).
19. Wang, F. et al. Implementing digital computing with DNA-based switching circuits. *Nat. Commun.* **11**, 121 (2020).
20. Wang, K. et al. Autonomous DNA nanomachine based on cascade amplification of strand displacement and DNA walker for detection of multiple DNAs. *Biosens. Bioelectron.* **105**, 159–165 (2018).
21. You, M., Zhu, G., Chen, T., Donovan, M. J. & Tan, W. Programmable and multiparameter DNA-based logic platform for cancer recognition and targeted therapy. *J. Am. Chem. Soc.* **137**, 667–674 (2015).
22. Zhu, J., Zhang, L., Zhou, Z., Dong, S. & Wang, E. Aptamer-based sensing platform using three-way DNA junction-driven strand displacement and its application in DNA logic circuit. *Anal. Chem.* **86**, 312–316 (2014).
23. Chen, Y. et al. A DNA logic gate based on strand displacement reaction and rolling circle amplification, responding to multiple low-abundance DNA fragment input signals, and its application in detecting miRNAs. *Chem. Commun.* **51**, 6980–6983 (2015).
24. Song, T. et al. Fast and compact DNA logic circuits based on single-stranded gates using strand-displacing polymerase. *Nat. Nanotechnol.* **14**, 1075–1081 (2019).
25. Shah, S. et al. Using strand displacing polymerase to program chemical reaction networks. *J. Am. Chem. Soc.* **21**, 9587–9593 (2020).
26. Douglas, S. M., Bachelet, I. & Church, G. M. A logic-gated nanorobot for targeted transport of molecular payloads. *Science* **335**, 831–834 (2012).
27. Kang, H. et al. DNA dynamics and computation based on toehold-free strand displacement. *Nat. Commun.* **12**, 4994 (2021).
28. Wang, D. et al. Molecular logic gates on DNA origami nanostructures for microRNA diagnostics. *Anal. Chem.* **86**, 1932–1936 (2014).
29. Yehl, K. et al. High-speed DNA-based rolling motors powered by RNAseH. *Nat. Nanotechnol.* **11**, 184–190 (2016).
30. Bazrafshan, A. et al. Tunable DNA origami motors translocate ballistically over μm distances at nm/s speeds. *Angew. Chem. Int. Ed.* **59**, 9514–9521 (2020).
31. Credi, A., Balzani, V., Langford, S. J. & Stoddart, J. F. Logic operations at the molecular level. An XOR gate based on a molecular machine. *J. Am. Chem. Soc.* **119**, 2679–2681 (1997).
32. Hu, L., Lu, C.-H. & Willner, I. Switchable catalytic DNA catenanes. *Nano Lett.* **15**, 2099–2103 (2015).
33. Blanchard, A. T. et al. Highly polyvalent DNA motors generate 100+ pN of force via autochemophoresis. *Nano Lett.* **19**, 6977–6986 (2019).
34. McKinnon, K. M. Flow cytometry: an overview. *Curr. Protoc. Immunol.* **120**, 5.1.1–5.1.11 (2018).
35. Chatterjee, G., Dalchau, N., Muscat, R. A., Phillips, A. & Seelig, G. A spatially localized architecture for fast and modular DNA computing. *Nat. Nanotechnol.* **12**, 920–927 (2017).
36. Vashist, S. K., Mudanyali, O., Schneider, E. M., Zengerle, R. & Ozcan, A. Cellphone-based devices for bioanalytical sciences. *Anal. Bioanal. Chem.* **406**, 3263–3277 (2014).
37. Ghonge, T. et al. Smartphone-imaged microfluidic biochip for measuring CD64 expression from whole blood. *Analyst* **144**, 3925–3935 (2019).

Methods

Materials. All chemicals were purchased from Sigma-Aldrich and used without further purification unless otherwise noted. All oligonucleotides were purchased from Integrated DNA Technologies, stored at 4 °C (−20 °C for RNA) and used without purification. Their sequences, including functional group modifications, are shown in Supplementary Table 1. Stock solutions were prepared using Nanopure water (Barnstead Nanopure System, resistivity = 18.2 MΩ), herein referred to as DI water. Aminated beads were obtained commercially: 5 μm aminated silica beads were purchased from Bangs Laboratory (SA06N), and 3 μm aminated polystyrene beads and 6 μm aminated polystyrene beads were purchased from Spherotech (ASIP-10-10 and AP-60-10). RNaseH was obtained from Takara Clontech (2150A). Thin Au films were generated using a home-built thermal evaporator system. All motor translocation measurements were performed in ibidi sticky-Slide VI0.4 17 × 3.8 × 0.4 mm³ channels. The smartphone microscope was obtained from W. Lam, Emory University (×10/0.25 numerical aperture (NA) objective and ×20 wide-field eyepiece; https://cellscope.berkeley.edu/).

Microscopy. Bright-field and fluorescence images were acquired on a fully automated Eclipse Ti2-E Nikon Inverted Research Microscope using the Elements software package (Nikon), an automated scanning stage, a 1.49 NA CFI Apo TIRF ×100 objective, a 0.50 NA CFI60 Plan Fluor ×20 objective, a Prime 95B 25 mm scientific complementary metal oxide semiconductor (sCMOS) camera for image capture at 16-bit depth, a SOLA SE II 365 Light Engine as a solid-state white-light excitation source and a perfect focus system used to minimize drift during time-lapse. Fluorescence images of cyanine dyes Cy3, Cy5 and fluoresceindye FAM were collected using a TRITC filter set (Chroma, 96321), an EGFP/FITC/Cy2/Alexa Fluor 488 filter set (Chroma, 96226) and a Cy5/Alexa Fluor 647/Draq 5 filter set (Chroma, 96232) with an exposure time of 100 ms. All imaging was conducted at room temperature.

Thermal evaporation of gold films. A No. 1.5H ibidi glass coverslip with dimensions 25 × 75 mm² (10812) was cleaned by sonication in DI water for 5 min. The sample was then subjected to a second sonication in fresh DI water for 5 min. Finally, the slide was sonicated in 200 proof ethanol (Fisher Scientific, 04-355-223) for 5 min and subsequently dried under a stream of N₂. The cleaned glass coverslip was then mounted in a home-built thermal evaporator chamber in which the pressure was reduced to 50×10^{-3} torr. The chamber was purged with N₂ three times and the pressure was reduced to $(1–2) \times 10^{-7}$ torr using a turbo pump with a liquid N₂ trap. Once the desired pressure had been achieved, a 3-nm film of Cr was deposited onto the slide at a rate of 0.2 Å s⁻¹, which was determined by a quartz crystal microbalance. After the Cr adhesive layer had been deposited, 6-nm layer of Au was deposited at a rate of 0.4 Å s⁻¹. The Au-coated samples were used within 1 week of deposition.

Fabrication of RNA monolayers. An ibidi sticky-Slide VI⁰·⁴ flow chamber (ibidi, 80608) was adhered to the Au-coated slide to produce six channels (17 × 3.8 × 0.4 mm³). Prior to surface functionalization, each channel was rinsed with ~5 ml DI water. Next, thiol-modified DNA anchor strands were added to each of the channels using a 50 μl solution of 1 μM DNA anchor in 1 M KHPO₄ buffer. The gold film was sealed with Parafilm to prevent evaporation, with the reaction taking place overnight at room temperature. After incubation, excess DNA was removed from the channels by rinsing with ~5 ml DI water. To block any bare gold sites and to maximize the hybridization of RNA to the DNA anchoring strands, the surface was backfilled with 100 μl of a 100 μM solution of 11-(mercaptoundecyl) hexa(ethylene glycol) (SH-PEG; Sigma-Aldrich, 675105) solution in ethanol for 6 h. Excess SH-PEG was removed by rinsing with ~5 ml ethanol followed by ~5 ml water. For a 1% surface-lock DNA surface, the RNA/DNA chimera F (99 nM) and surface-lock DNA D* (1 nM) were mixed and added to the surface through hybridization in 1× PBS for 12 h. In addition, for a 5% surface-lock DNA surface, the RNA/DNA chimera F (95 nM) and the surface-lock DNA D* (5 nM) were mixed and added to the surface through hybridization in 1× PBS for 12 h. The channels were again sealed with Parafilm to prevent evaporation and the resulting RNA monolayer remained stable for days.

Synthesis of azide-functionalized DMOLs. Before functionalization with azide, the aminated silica and polystyrene beads were washed to remove any impurities as follows: 1 mg aminated silica beads were washed by centrifugation for 5 min at 15,000 r.p.m. in 1 ml DI water, and 1 mg aminated polystyrene beads were centrifuged for 10 min at 15,000 r.p.m. in 1 ml DI water containing 0.005% Triton-X surfactant. The supernatant was discarded, and the resulting particles were resuspended in 1 ml DI water (silica beads) and 1 ml DI water containing 0.005% Triton-X (polystyrene beads). This was repeated three times and the supernatant was discarded after the final wash. The azide-functionalized particles were then synthesized by mixing 1 mg aminated silica or polystyrene beads with 1 mg azidoacetic *N*-hydroxysuccinimide ester (BroadPharm, BP-22467). This mixture was subsequently diluted in 100 μl dimethylsulfoxide (DMSO) and 1 μl of a tenfold-diluted triethylamine stock solution in DMSO. The reaction was allowed to proceed for 24 h at room temperature. The resulting azide-modified silica particles were then purified by adding 1 ml DI water and centrifuging the particles at

15,000 r.p.m. for 5 min. The azide-modified polystyrene particles were purified in a similar manner, except they were centrifuged for 10 min in 0.005% Triton-X. The supernatant was discarded and the resulting particles were resuspended in 1 ml DI water. This process was repeated seven times, and after the final centrifugation step the particles were resuspended in 100 μl DI water to yield an azide-modified particle stock. The azide-modified particles were stored at 4 °C in the dark and used within 1 month of preparation.

Synthesis of high-density DNA-functionalized silica and polystyrene DMOLs. High-density DNA-functionalized particles were synthesized by adding a total of 5 nanomoles (in 5 μl) of alkyne-modified DNA stock solution to 5 μl of azide-functionalized particles. For DMOL1, 2.5 nanomoles of guide DNA G and 2.5 nanomoles of particle-lock C* were mixed with 5 μl of azide-functionalized silica particles. For DMOL2, 2.5 nanomoles of guide DNA G and 1.25 nanomoles (each) of particle-lock C* and M* were mixed with 5 μl of azide-functionalized polystyrene particles. For DMOL3, 4.5 nanomoles of guide DNA G and 0.5 nanomoles of particle-lock C* were mixed with 5 μl of azide-functionalized polystyrene particles. For DMOL4, 3.5 nanomoles of guide DNA G and 1.5 nanomoles of particle-lock C* were mixed with 5 μl of azide-functionalized silica particles. For DMOL5, 4.5 nanomoles of guide DNA G and 0.5 nanomoles of particle-lock M* were mixed with 5 μl of azide-functionalized silica particles. For DMOL6, 2.5 nanomoles of guide DNA G and 0.83 nanomoles (each) of particle-lock C*, M* and P* were mixed with 5 μl of azide-functionalized polystyrene particles. The particles and DNA were diluted with 25 μl DMSO and 5 μl of 2 M triethylammonium acetate buffer. Next, 4 μl of a supersaturated stock solution of ascorbic acid was added to the reaction as a reducing agent. Cycloaddition between the alkyne-modified DNA and azide-functionalized particles was initiated by adding 2 μl of a 10 mM copper tris[(1-benzyl-1*H*-1,2,3-triazol-4-yl)methyl]amine (Cu-TBTA) stock solution in 55 vol% DMSO (Lumiprobe, 21050). The reaction was incubated for 24 h at room temperature on a shaker and the resulting DNA-functionalized particles were purified by centrifugation. The particles were centrifuged at 15,000 r.p.m. for 10 min, after which the supernatant was discarded and the particles resuspended in 1 ml of a 1× PBS and 10% Triton-X (w/v) solution. This process was repeated seven times, with the particles resuspended in 1 ml of 1× PBS only for the fourth to sixth centrifugations. After the final centrifugation, the particles were resuspended in 50 μl of 1× PBS buffer. The high-density DNA-functionalized particles were stored at 4 °C and protected from light.

For modification with the staple-lock DNA strands, 10 μl of DNA-functionalized particles (DMOL1–3, DMOL5 and DMOL6) were diluted in 1× PBS with 100 nM of staple-lock DNA. DMOL4 was diluted in the same manner but with 500 nM of staple-lock DNA. The solutions were vortexed and incubated overnight at room temperature. The particles were then washed by centrifugation at 15,000 r.p.m for 10 min in 1 ml of 1× PBS. The supernatant was discarded and the resulting particles were resuspended in 1 ml of 1× PBS. This process was repeated three times, and after the final centrifugation step the particles were resuspended in 50 μl of 1× PBS. The staple-lock-modified particles were then stored at 4 °C in the dark.

Particle translocation. Before beginning experiments, RNA–substrate surfaces were washed with 5 ml of 1× PBS to remove excess unbound RNA. The quality of the RNA monolayer in each well was checked for homogeneity and intensity (~10,000 intensity units is typical). Next, DNA-functionalized particles were hybridized to the RNA substrate. This was achieved by diluting 5 μl of DNA-functionalized particles in 45 μl of 1× PBS. Hybridization between the particles and the complementary RNA/surface-lock DNA monolayer occurred over an incubation period of 10 min. After hybridization, the surface was gently washed with 1× PBS to remove any unbound particles. Particle translocation was then initiated by adding rolling buffer consisting of water (77.5%), formamide (10%), 10% Triton-X (w/v) in water (7.5%) and 10× RNaseH buffer (5%, consisting of 500 mM Tris-HCl, 750 mM KHPO₄ and 3 mM MgCl₂, pH 8.0). RNaseH and dithiothreitol (DTT) were then added to the rolling buffer: 1 μl of the RNAseH stock solution was diluted in 23 μl of 500 μM DTT in 1× PBS and stored on ice for up to 2 h (1 μl of this dilution contains 5 U RNaseH). A similar protocol was followed for the 3 μm particles, except that the rolling buffer contained 15% of 10× RNaseH buffer rather than 5%. Particle tracking was achieved through bright-field imaging by time-lapse acquisition at intervals of 5 s for 30 min using the Nikon Elements software. High-resolution epifluorescence images (×100) of the fluorescence-depletion tracks and particle fluorescence intensity were acquired to verify that particle motion resulted from processive RNA hydrolysis and confirm the TMSD reaction. The resulting time-lapse files and high-resolution epifluorescence images were then saved for further analysis.

Image processing and particle tracking. Image processing and particle tracking were performed in Fiji (ImageJ) as well as in Python. The bioformats toolbox enabled direct transfer of Nikon Elements image files (*.nd2) into the Fiji (ImageJ) environment where all image/video processing was performed. The algorithms for processing the data for motor trajectories, net displacements and speeds were performed on Python (v. 3.7.4). Calculation of drift correction was adapted from trackpy (https://soft-matter.github.io/trackpy/v0.4.2/). Full Python script from

bright-field acquisition data can be found at https://github.com/spiranej/particle_tracking_. Statistical analyses were performed in GraphPad (v. 9.1.0).

Data availability

Code availability

Python script from bright-field acquisition data regarding net displacements and particle ensemble trajectories can be found at https://github.com/spiranej/particle_tracking_.

Acknowledgements

Author contributions

S.P. conceptualized the project, designed all experiments, analysed the data and compiled the figures. A.B. helped in the data analysis and discussion of the data. K.S. conceptualized and supervised the project. S.P. and K.S. wrote the manuscript with contributions from A.B.

Competing interests

The authors declare no competing interests.

Additional information

Supplementary information The online version contains supplementary material available at https://doi.org/10.1038/s41565-022-01080-w.

Correspondence and requests for materials should be addressed to Khalid Salaita.

Peer review information *Nature Nanotechnology* thanks Eyal Nir, Zhisong Wang and the other, anonymous, reviewer(s) for their contribution to the peer review of this work.

Reprints and permissions information is available at www.nature.com/reprints.